


Mismatched atomic bonds and ultralow thermal conductivity in Ag-based ternary chalcopyritesRuoyu Wang,^{1,2} Jianfeng Cai ,^{1,2} Qiang Zhang,^{1,2} Xiaojian Tan,^{1,2} Jiehua Wu,¹ Guoqiang Liu,^{1,2,*} and Jun Jiang^{1,2,†}¹Ningbo Institute of Materials Technology and Engineering, Chinese Academy of Sciences, Ningbo 315201, China²College of Materials Science and Opto-Electronic Technology, University of Chinese Academy of Sciences, Beijing 100049, China

(Received 1 November 2022; revised 8 January 2023; accepted 23 February 2023; published 10 March 2023)

Diamond like ternary chalcopyrites MBX_2 ($M = \text{Cu, Ag}$; $B = \text{Ga, In, Tl}$; $X = \text{S, Se, Te}$) have attracted tremendous research interest in thermoelectric society due to the competitive performance and a great variety of transport properties. Interestingly, the lattice thermal conductivity of $AgBX_2$ is systematically two to five times lower than that of $CuBX_2$, in spite of their similar crystal and band structures. Based on the careful theoretical analysis, we show that the ultralow thermal conductivity of $AgBX_2$ originates in the mismatched atomic bonds between Ag-X and B-X pairs. Owing to the very expanded $4d$ orbital of Ag, the bonding strength of Ag-X is much weaker than that of B-X. As a result, the vibrations of Ag-X and B-X are well separated within the low-frequency modes. The phonon density of states of $AgBX_2$ exhibits four divided peaks, compared with the three peaks in $CuBX_2$. The calculated joint phonon density of states reveals that such characteristic in $AgBX_2$ would increase the scattering rate of low-frequency phonons significantly. This study provides essential understandings on the ultralow thermal conductivity of Ag-based ternary chalcopyrites and indicates a general strategy to suppress the thermal conductivity in ternary compounds.

DOI: [10.1103/PhysRevB.107.115202](https://doi.org/10.1103/PhysRevB.107.115202)**I. INTRODUCTION**

Thermoelectric (TE) materials directly convert heat into electricity, and thus provide an option for green energy [1]. The energy conversion efficiency of a TE material can be measured by a dimensionless figure of merit, $ZT = S^2\sigma T/\kappa$, where S , σ , T , and κ represent Seebeck coefficient, electrical conductivity, temperature, and thermal conductivity, respectively. Usually, the thermal conductivity κ can be further divided into the electronic (κ_e) and lattice (κ_l) parts. An ideal TE material with high ZT requires low κ , high S , and high σ [2]. A central focus of the TE community has been the improvement of overall ZT of potential thermoelectric materials, e.g., Bi_2Te_3 , PbTe , Mg_3Sb_2 , etc. [3–7]. Since κ_e is strongly coupled with σ , thermoelectric materials with intrinsic low lattice thermal conductivity are highly desired. In recent years, diamondlike ternary chalcopyrites of MBX_2 -type ($M = \text{Cu, Ag}$; $B = \text{Al, Ga, In}$; $X = \text{S, Se, Te}$) have drawn lots of research interest for their competitive TE performance and varied transport behaviors [8–13]. In such compounds, each M or B cation forms a tetrahedron with the four nearest-neighbor anions. With proper optimization, MBX_2 compounds can achieve high ZT values. For example, by Ag and In alloying, the p -type $\text{Cu}_{0.8}\text{Ag}_{0.2}\text{In}_{0.2}\text{Ga}_{0.8}\text{Te}_2$ synthesized by Xie *et al.* reached a maximum ZT of 1.5 at 850 K [11]. Another example was the n -type AgInSe_2 reported by Zhu *et al.* [14]. A high ZT of 1.2 at 800 K was obtained after delicate Na addition and vacancy control [14]. Despite the general similarity in crystal structures, members of MBX_2

chalcopyrites exhibit distinct physical properties. In a previous work by Cao *et al.*, the lattice structures and transport properties of $MB\text{Te}_2$ ($M = \text{Ag, Cu}$, $B = \text{Ga, In}$) were measured [15]. Both AgGaTe_2 and AgInTe_2 exhibit an extremely low room temperature κ around $1.4 \text{ W m}^{-1} \text{ K}^{-1}$. On the contrary, CuGaTe_2 and CuInTe_2 have much higher κ values of 6.7 and $5.9 \text{ W m}^{-1} \text{ K}^{-1}$, respectively. This stark contrast in κ between Ag- and Cu-based compounds is almost universal among the MBX_2 chalcopyrites family. Besides the low κ , Ag(Ga, In)Te_2 also exhibits low intrinsic hole concentration in the order of 10^{15} cm^{-3} at room temperature, whereas that of Cu(Ga, In)Te_2 reached 10^{18} cm^{-3} .

To explain the remarkable difference between Ag- and Cu-based chalcopyrites, especially the extremely low κ of $AgBX_2$, extensive research efforts have been made. Zhu *et al.* executed a comprehensive inelastic neutron scattering measurement on AgInSe_2 , verifying the presence of strong anharmonicity and the “avoid-crossing” feature in phonon spectrum [16]. The authors further conclude that the above phenomenon is closely associated with the weakly bound Ag atom. Though valuable insights are provided, the exact relation between Ag vibration and low κ needs to be clarified. More recently, via a combined experimental and theoretical approach, Xie *et al.* made a comparative study on AgGaTe_2 and CuGaTe_2 [17]. In their opinion, the Ag off-centering distortion in the AgTe_4 tetrahedron breaks the local symmetry, which was believed to be responsible for the much lower κ_l in AgGaTe_2 than in CuGaTe_2 . The weak sd^3 hybridization in the tetrahedral Ag atoms, owing to the large energy difference between Ag- $4d$ and Ag- $5s$ orbitals, was claimed to be the driving force of Ag displacement. Though the authors succeeded in relating the low κ_l to the features of electronic structures, it is worth noting that Ag has a filled $4d$ shell and the concept of sd^3

*liuqg@nimte.ac.cn

†jjun@nimte.ac.cn

hybridization raised here is doubtful. Moreover, the claimed explanation seems not to be universal for all AgBX_2 , as the members exhibit a similar lattice thermal conductivity in spite of their very different structural distortions [15,18].

In this work, the puzzling low thermal conductivity AgBX_2 is clarified based on the careful analyses of electronic band structures. We identified that the different bonding strength between $M-X$ and $B-X$, or mismatched bond, is critical to the thermal transport. In Ag-based compounds, the Ag-X bond is much weaker than the $B-X$ bond, mainly due to the very expanded Ag- $4d$ orbital. As a result, low-frequency phonon modes are dominated by the Ag-X vibration, leading to the significant increase of the three-phonon scattering processes and then the ultralow κ_l . On the contrary, due to the similar bonding strength between Cu-X and $B-X$, the κ_l of Cu-based chalcopyrites are much higher. The above understanding explains the effectiveness of minor Ag alloying in suppressing the κ_l of Cu-based ternary chalcopyrites and provides insight into the design of thermoelectric materials with low κ_l .

II. THEORETICAL METHODS

First-principles energy calculations were performed within the framework of density functional theory (DFT) as implemented by the VASP codes. The projector-augmented wave function of PBE (Perdew-Burke-Ernzerhof) form and GGA (generalized gradient approximation) type exchange-correlation potential were utilized for the DFT calculation [19]. Electronic density of states was calculated based on relaxed conventional unit cells with experimental lattice constants, using a cut-off energy of 400 eV and a gamma-centered $9 \times 9 \times 5$ k -point grid. On the other hand, primitive cells were used for the electronic band structure calculation. Since the GGA type exchange-correlation potential tends to severely underestimate the energy gap, we deployed the modified Becke-Johnson method in band structure calculation [20]. Thermal conductivity was calculated using $2 \times 2 \times 1$ supercells of the conventional unit cell with a Monkhorst-Pack k -point grid of $4 \times 4 \times 4$, which consists of 64 atoms. Since phonon-phonon scattering dominates thermal transport in semiconductors, only lattice thermal conductivity was considered. For phonon properties, the finite displacement method (FDM) as implemented in PHONOPY code was used to calculate the second-order (harmonic) interatomic force constants (IFCs) by energy derivatives [21,22]. The harmonic IFCs were then transformed into dynamical matrices in reciprocal space, and the phonon dispersion curves can be obtained by diagonalizing the dynamical matrices. To describe anharmonicity in phonon transport, the atomic interaction was considered up to the third order. The third-order IFCs were deduced from the same FDM, and the room temperature thermal conductivity of CuInTe_2 is 9.29, 8.12, and 8.03 $\text{W m}^{-1} \text{K}^{-1}$ for considering up to the first-, second-, and third-nearest-neighbor IFCs, respectively. Therefore, third-order IFCs up to the second-nearest neighbor should be sufficient to capture the essential atomic interactions. Using harmonic and anharmonic IFCs as input, the thermal conductivity was derived within the framework of the SHENGBTE package by solving the linearized semiclassical phonon Boltzmann transport equation (phonon BTE) with relaxation-time approximation

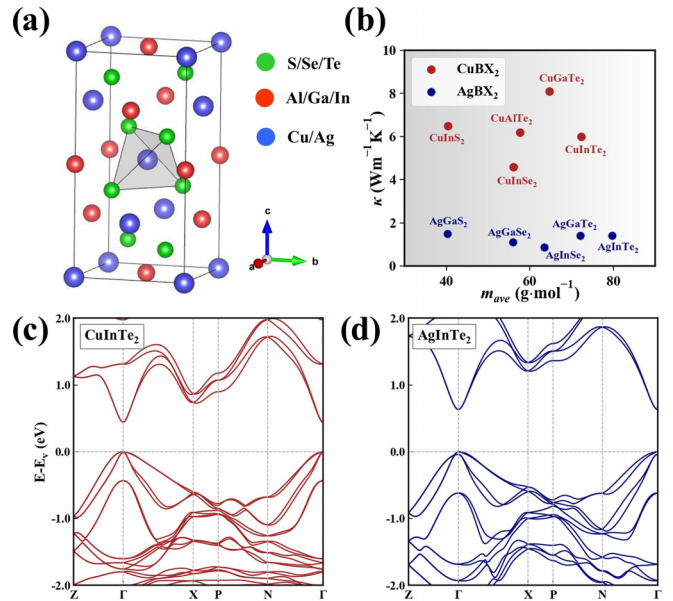


FIG. 1. Crystal structure, thermal conductivity, and electronic band structure of ABX_2 chalcopyrite. (a) Conventional unit cell of the $M\text{InTe}_2$ ($M = \text{Cu}, \text{Ag}$) compound. (b) Experimental room temperature thermal conductivity of ABX_2 compounds [15,27–30]. (c) Electronic band structure of (c) CuInTe_2 and (d) AgInTe_2 .

[23]. In the framework of phonon BTE, phonons are treated as semiclassical particles with group velocity being extracted from phonon dispersion. The mode-specific relaxation time due to the three-phonon scattering process can be obtained from the third-order IFCs. It should be noted that both normal and umklapp processes contribute to the relaxation time, and such relaxation-time approximation may slightly underestimate thermal conductivity [24,25]. A dense q -point grid of $10 \times 10 \times 10$ was applied to calculate lattice thermal conductivity, and convergence tests on CuInTe_2 show that the calculated room temperature thermal conductivity was 0.36 $\text{W m}^{-1} \text{K}^{-1}$ lower for the $8 \times 8 \times 8$ grid and only 0.07 $\text{W m}^{-1} \text{K}^{-1}$ higher for the $12 \times 12 \times 12$ grid. The joint phonon density of states was calculated by a home-grown program in conjunction with SHENGBTE, using phonon calculation results from PHONOPY as input.

III. RESULTS AND DISCUSSION

A. Crystal and electronic band structures

Chalcopyrite MBX_2 assumes a CuFeS_2 -type structure with $I42m$ point group, whereas each cation atom forms a tetrahedron with the four neighboring anion atoms. Figure 1(a) presents the conventional unit cell of MBX_2 compounds, which consists of an equal number of tetrahedrons centered around the M and B cation atoms. An illustration of the tetrahedron can also be found in the Supplemental Material [26]. Figure 1(b) relates the experimental thermal conductivity κ of various MBX_2 compounds to their respective average atomic masses m_{ave} [15,27–30]. According to the empirical theory, lattice thermal conductivity is proportional to m_{ave} [31]. The κ of CuBX_2 however, are systematically two to five times higher

TABLE I. The experimental lattice parameter of various MBX_2 compounds [32–35].

Compounds	a (Å)	c (Å)	$\eta = c/2a$
CuInTe ₂	6.17	12.34	1.000
CuGaTe ₂	5.99	11.91	0.994
CuAlTe ₂	6.04	11.94	0.988
CuInSe ₂	5.77	11.55	1.001
CuInS ₂	5.52	11.13	1.008
AgInTe ₂	6.41	12.56	0.981
AgInSe ₂	6.09	11.67	0.958
AgGaTe ₂	6.30	11.97	0.950
AgGaSe ₂	5.97	10.88	0.911
AgGaS ₂	5.74	10.26	0.894

than that of $AgBX_2$, regardless of mass difference. Thus, the heavier mass of Ag cannot account for the low κ .

Table I lists experimental lattice parameters a and c , and $c/2a$ ratio η of various MBX_2 chalcopyrites [32–35]. The calculated lattice parameters are also given in Supplemental Material Table S1, which fit well with experimental results. The η of most $CuBX_2$ is very close to the unity, whereas $AgBX_2$ has smaller η and larger lattice parameter. In principle, the η value deviates from unity if the lattice is distorted, and thus the $AgBX_2$ compounds have the more distorted structures. In a recent work, Xie *et al.* claimed the local symmetry breaking, which manifests in lattice distortion, is responsible for the low κ of $AgBX_2$ [17]. In their work, the absolute value of $(1 - \eta)$ was used to denote the structural distortion. According to Table I, the η value of 0.950 for $AgGaTe_2$ is indeed much smaller than that of 0.994 for $CuGaTe_2$. The much lower κ of $AgGaTe_2$ than $CuGaTe_2$ seems to support the authors' conclusion. However, $AgInTe_2$ has an η value of 0.981, which is much larger than that of $AgGaTe_2$. Despite the much less distorted structure, $AgInTe_2$ still exhibits an extremely low κ of $1.4 \text{ W m}^{-1} \text{ K}^{-1}$, almost the same as $AgGaTe_2$. On the other hand, $AgGaS_2$ has a much stronger structural distortion than $AgGaTe_2$, whereas it also exhibits a similar thermal conductivity of $1.5 \text{ W m}^{-1} \text{ K}^{-1}$ [27]. Therefore, the claimed local structural distortion may not be the universal explanation for the extremely low κ of $AgBX_2$. To explain the origin of low κ , we need to investigate the detailed electronic structure of the MBX_2 family.

To compare the electronic structure of Ag- and Cu-based chalcopyrites, $AgInTe_2$ and $CuInTe_2$ are chosen for the representative compounds. Figures 1(c) and 1(d) present the electronic band structure of $CuInTe_2$ and $AgInTe_2$, respectively. Since the exchange-correlation potential in the GGA often significantly underestimates the band gap, we employ the modified Becke Johnson potential instead. The spin-orbit coupling effect is also considered due to the presence of heavy cation atoms, i.e., Te. Based on the electronic band calculation, both compounds are direct-gap semiconductors with valence and conduction band edges set at the Γ point in the Brillouin zone (BZ). As may be seen, $CuInTe_2$ and $AgInTe_2$ exhibit very similar band structures. Considering the very different lattice thermal conductivities between $CuInTe_2$ and $AgInTe_2$, their similar electronic band dispersions are somehow unexpected.

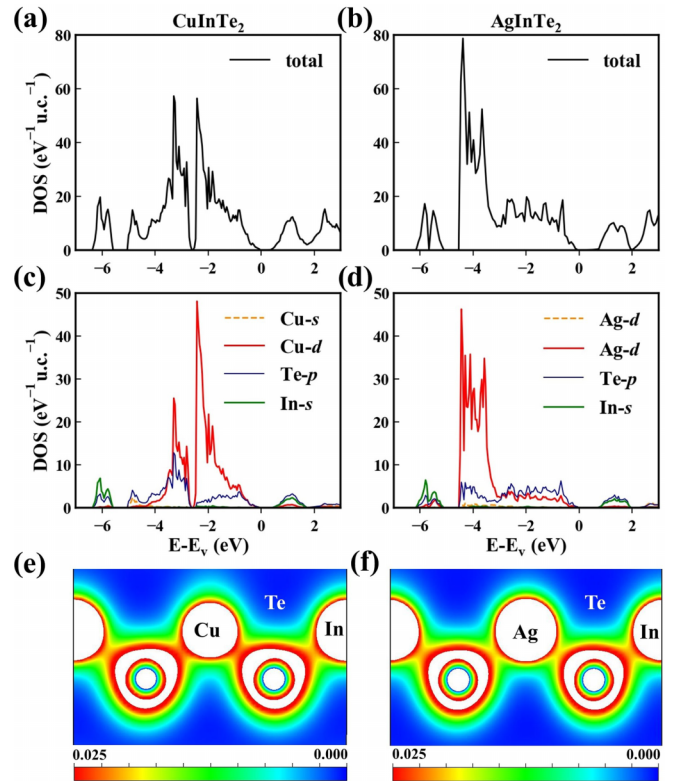


FIG. 2. Total electronic density of state (DOS) for $CuInTe_2$ (a) and $AgInTe_2$ (b), respectively. Projected DOS of $CuInTe_2$ (c) and $AgInTe_2$ (d), respectively. Real-space electron density at the (110) plane of $CuInTe_2$ (e) and $AgInTe_2$ (f), respectively.

B. Electronic structure analysis

To get an insight into the band structures, both total and orbital projected density of states (DOS and PDOS) of $AgInTe_2$ and $CuInTe_2$ are presented in Fig. 2. As shown in Figs. 2(a) and 2(b), the total DOS of $CuInTe_2$ is very different from that of $AgInTe_2$. From 0 to -5 eV, $CuInTe_2$ shows two well-separated peaks, whereas $AgInTe_2$ shows one main peak around -4 eV. The PDOS in Fig. 2(c) indicates that the mentioned two peaks of $CuInTe_2$ are mainly from Cu-3d orbital. Meanwhile, a strong overlap between the Cu-3d and Te-p orbitals can be observed at the valence band edge and around -3 eV. This phenomenon suggests the covalentlike bonding between Cu-3d and Te-p orbitals, and thus the two peaks of Cu-3d can be attributed to the separation of the bonding and antibonding states. At -6 and 1 eV, a large overlap between the Te-p and In-s orbitals can be observed as well, indicating the strong covalent bonding between the two orbitals.

As shown in Fig. 2(d), the Ag-d orbital in $AgInTe_2$ exhibits a very different distribution from the Cu-d orbital in $CuInTe_2$. From 0 to -5 eV, the Te-p PDOS is weakly related to the Ag-d PDOS, while no sharp peak for the Te-p orbital can be observed. Contrary to $CuInTe_2$, the calculated PDOS suggests the weak bonding between the Ag-d and Te-p orbitals. For this reason, the p-d bonding and antibonding states are not well separated, and therefore the Ag-d orbital only exhibits one main peak. On the other hand, the covalent bonding between the Te-p and In-s orbitals is similar to that in $CuInTe_2$.

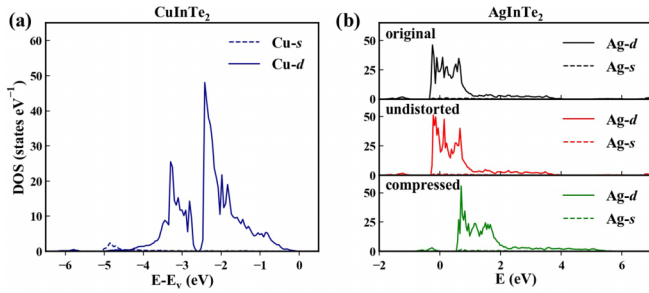


FIG. 3. The Cu-projected density of states for pristine CuInTe₂ and AgInTe₂ of original, undistorted, and compressed lattice, respectively. (a) Cu-projected density of states (PDOS) of CuInTe₂. Calculated DOS of AgInTe₂ using (b) original unit cell, (c) a standard diamond unit cell of the same volume, and (d) a compressed unit cell, respectively.

The bond strength of covalent bonding can be visualized by the electron distribution in real space. Figures 2(e) and 2(f) present the electron density within the (110) plane for CuInTe₂ and AgInTe₂, respectively. In CuInTe₂, both Cu-Te and In-Te pairs show the strong covalent bonds, as indicated by the high electron density between the atomic spheres. In AgInTe₂, however, the bonding strength between Ag-Te is obviously weaker than that between In-Te. The calculated electron densities in real space are consistent with our analyses for the energetic band structures.

The weaker *p-d* bonding in AgBX₂ than in CuBX₂ has been revealed in some previous studies [18,36]. It was believed that the lower Ag-*d* orbital level than the Cu-*d* orbital is responsible for the weaker bonding strength in AgBX₂. Based on this conclusion, Xie *et al.* further argued that the weak *p-d* bonding causes the Ag off-centring distortion in the AgTe₄ tetrahedron, resulting in the local symmetry breaking and the ultralow lattice thermal conductivity in AgGaTe₂ [17]. Within the valence-bond theory framework, the authors attributed the structural distortion to the decreased *sd*³ hybridization. According to our discussions, the strength of the *p-d* bonding is reflected in the PDOS of the Cu/Ag-*d* orbital. To disclose the origin of the weak *p-d* bonding in AgBX₂, we calculated the Ag-projected DOS within two artificial structures of AgInTe₂, as shown in Fig. 3.

Firstly, we examine the relationship between *p-d* bonding strength and the local structural distortion. Using the ideal tetrahedral structure with the constant volume, the calculated Ag-projected DOS in AgInTe₂ is presented in Fig. 3(b). As may be seen, the local structural distortion in AgInTe₂ shows little influence on the Ag-projected DOS. Secondly, we consider the effect of the energy level of the Ag-*d* orbital. If the crystal volume is compressed, the Ag-*d* orbital could be upwards shifted by the increased crystal field [37]. The calculated Ag-projected DOS within 5% compressed structure is presented in Fig. 3(b). The figure shows that the Ag-*d* orbital is indeed upwards shifted, but its distribution is still very different from that of the Cu-*d* orbital in CuInTe₂. This result indicates that the *p-d* bonding in AgInTe₂ cannot be simply enhanced by raising the *d*-orbital level. In the framework of tight-binding theory, the bond strength between two orbitals depends on the energy difference of orbital levels and the

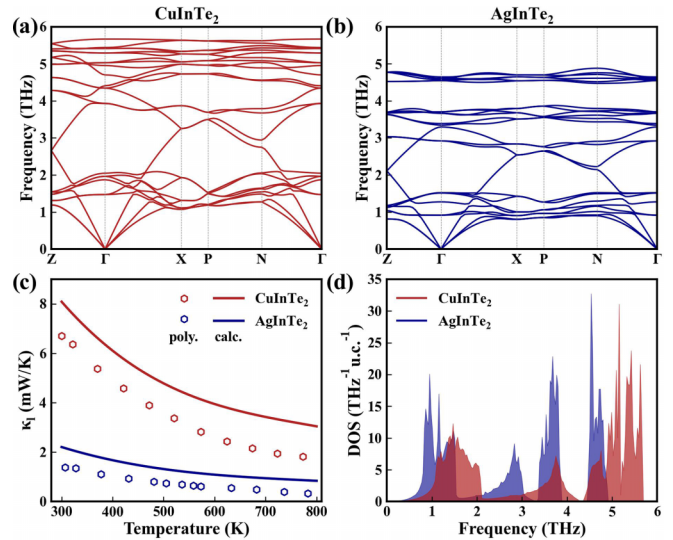


FIG. 4. The lattice vibration properties of AgInTe₂ and CuInTe₂. Phonon dispersion of (a) CuInTe₂ and (b) AgInTe₂. (c) Calculated lattice thermal conductivity of CuInTe₂ and AgInTe₂. (d) Calculated phonon density of states of CuInTe₂ and AgInTe₂.

hopping integral [38]. Thus, the low hopping integral in AgInTe₂ becomes the exclusive reason for the weak *p-d* bonding. Compared with the Cu-3*d* orbital, Ag-4*d* is much more expanded in real space, which rationalizes the low hopping integral between the Ag-*d* and Te-*p* orbitals. Our discussion reveals that the weak *p-d* bonding in AgBX₂ is actually element dependent. In the Supplemental Material, the calculated PDOS for different AgBX₂ compounds are presented. One may find that they all show a similar Ag distribution to AgInTe₂.

Besides the origin of *p-d* bonding strength, the PDOS analysis also discloses some electronic transport features. Figures 2(c) and 2(d) indicate that the *p*-type transport is mainly determined by the *M*-Te conductive network, and the *n*-type transport by the *B*-Te conductive network [39,40]. This observation may be helpful for the design of high entropy structures. In a previous study on *p*-type CuInTe₂, it was found that the solid solution at the “In” site can decrease the lattice thermal conductivity significantly while the influence on electrical conductivity was relieved [41].

C. Phonon spectra and lattice thermal conductivity

Figures 4(a) and 4(b) present the calculated phonon spectra of AgInTe₂ and CuInTe₂, respectively. The two spectra show similar phonon structures, except for the softer acoustic branches and lower optical branches for AgInTe₂, which may be due to the heavier mass of Ag. Supplemental Material Fig. S5 compares the calculated mode-specific sound velocity of the two compounds [26]. The acoustic sound velocity of AgInTe₂ is found to be roughly 1.5 times lower than that of CuInTe₂. Figure 4(c) presents the calculated thermal conductivity κ_l of AgInTe₂ and CuInTe₂ as well as the experimental values of polycrystalline samples [15,41]. The calculated κ_l of AgInTe₂ are almost five times lower than that of CuInTe₂, consistent with the experimental results. It

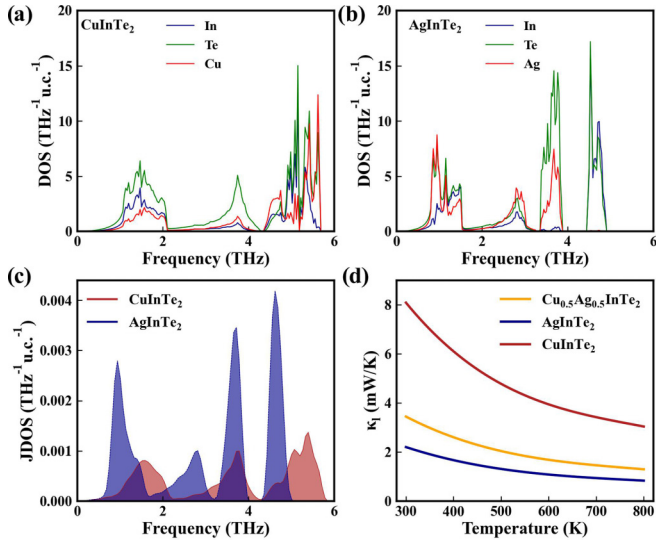


FIG. 5. Projected phonon density of states (PHDOS) and joint phonon density of states (JDOS) for CuInTe_2 and AgInTe_2 . PHDOS of CuInTe_2 (a) and AgInTe_2 (b), respectively. (c) JDOS of CuInTe_2 and AgInTe_2 . (d) Calculated κ_l of CuInTe_2 , AgInTe_2 , and the $\text{Cu}_{0.5}\text{Ag}_{0.5}\text{InTe}_2$ alloy.

is also worth noting that the calculated κ_l of AgInTe_2 along the c axis are almost 20% higher than that along a axis due to the strongly anisotropic structure, whereas the κ_l of CuInTe_2 are roughly homogeneous, as shown in Fig. S7(a) [26]. Apparently, the smaller sound velocity of AgInTe_2 cannot fully explain its ultralow thermal conductivity. It is conceivable that the phonon-phonon scattering rate in AgInTe_2 should be much larger, especially the acoustic branches. In Fig. 4(d), the calculated phonon density of states (PHDOS) for AgInTe_2 and CuInTe_2 are presented. The PHDOS of AgInTe_2 shows four separated peaks, compared with the three pieces in CuInTe_2 . The very different phonon distribution in AgInTe_2 and CuInTe_2 should relate to their different lattice thermal conductivity.

Figures 5(a) and 5(b) present the atom-projected PHDOS for CuInTe_2 and AgInTe_2 , respectively. In CuInTe_2 , as may be seen, the vibrations of Cu and In are nearly hybridized together. In AgInTe_2 , however, the vibrations of Ag-Te and In-Te pairs are well separated above 3 THz. At the low-frequency range (< 1 THz), the Ag-Te pair contributes a sharp PHDOS peak, which is absent in CuInTe_2 . Based on the analysis of electronic band structures, these differences between CuInTe_2 and AgInTe_2 are easy to understand. In AgInTe_2 , the bonding strength between the Ag-Te and In-Te pairs is very different, and therefore their vibrations are separated. The low-frequency sharp peak can also be simply attributed to the weak bonding of the Te-Ag pair.

To clearly show the connection between phonon modes and lattice thermal conductivity, the joint phonon DOS (JDOS) are calculated for CuInTe_2 and AgInTe_2 . It is defined as

$$\text{JDOS}^{\pm}(\omega) = (N_q)^{-3} \sum_{n,n'} \sum_{q,q'} \delta[\omega - \omega_n(q)] \times \delta[\omega_n(q) \pm \omega_{n'}(q') - \omega_{n'}(q \pm q' - G)],$$

where ω , n , and N_q represent phonon frequency, phonon branch, and the number of sampling points q within BZ, respectively. G is a reciprocal lattice vector that is zero for normal processes and nonzero for umklapp processes. The summation is over all sampled phonon modes and normalized by a factor of N_q^{-3} . The $\text{JDOS}^+(\omega)$ and $\text{JDOS}^-(\omega)$ corresponds to the “summation” and “difference” processes, respectively, and $\text{JDOS}(\omega)$ is the sum of the two processes

$$\text{JDOS}(\omega) = \text{JDOS}^+(\omega) + \text{JDOS}^-(\omega),$$

which measures the maximum possibility of the three phonon processes allowed by the law of energy and momentum conservation [42]. Thus, higher JDOS suggests the stronger three-phonon scattering and the lower κ_l . Figure 5(d) presents the calculated JDOS of CuInTe_2 and AgInTe_2 , respectively. As may be seen, the JDOS of AgInTe_2 shows a very sharp peak around 1 THz, which indicates the high scattering rate of acoustic phonon branches. Since the lattice thermal conductivity is mainly contributed by the acoustic branches, the JDOS peak naturally explains the ultralow thermal conductivity of AgInTe_2 . It is noticeable that the low-frequency JDOS peak of AgInTe_2 is mainly from the peak of phonon DOS, which originates in the much weaker bonding between Ag-Te than between In-Te. According to our discussions, the very expanded $4d$ orbital of Ag is responsible for the weak p - d bonding, and the influence of structural variation is insignificant. This is the reason why all the AgBX_2 show the ultralow thermal conductivity.

Despite the higher κ_l , CuBX_2 is in fact more favorable for p -type thermoelectric materials, owing to intrinsic high carrier concentration and high mobility. To suppress the excessively high κ_l of Cu-based TDCs, several strategies have been proposed and the alloying of minor Ag proved to be most effective among others. At a relatively low concentration (less than 20%), Ag alloying significantly lowered the κ_l with minor cost in electronic transportation [43]. To explain the surprisingly effective Ag alloying, Fig. S13(a) presents the calculated PHDOS of a simplified $\text{Cu}_{0.5}\text{Ag}_{0.5}\text{InTe}_2$ structure, as shown in Fig. S12 [26]. Upon Ag substitution, high-intensity PHDOS peaks dominated by Ag-Te vibration are introduced at around 1.0 and 3.7 THz, suggesting strong bond mismatch [44]. As a result, the JDOS of $\text{Cu}_{0.5}\text{Ag}_{0.5}\text{InTe}_2$, as presented in Fig. S13(b), increases significantly, resulting in stronger phonon scattering. Figure 5(d) provides the calculated κ_l of the three compounds. The κ_l of the $\text{Cu}_{0.5}\text{Ag}_{0.5}\text{InTe}_2$ phase almost drops to the same level as the pure AgInTe_2 . Therefore, the κ_l of CuInTe_2 can be significantly reduced even with minor Ag alloying.

IV. CONCLUSIONS

In summary, we have traced the ultralow κ_l of AgBX_2 to the mismatched bonds between the Ag- X and B - X pairs. This is a result of the much weaker Ag- d / X - p hybridization as the result of the broader real-space distribution of the Ag- $4d$ orbital. Owing to the bond mismatch, low-frequency phonon modes dominated by the Ag- X vibration are introduced, and it significantly enlarges the JDOS, suggesting the

high phonon-phonon scattering rate. On the contrary, the bond mismatch is much less apparent in CuBX_2 due to the stronger Cu-3d/ X - p bond. Consequently, the κ_l of CuBX_2 is significantly higher than their Ag-based counterparts. Following the above instruction, the effectiveness of Ag alloying in suppressing the κ_l of CuBX_2 can be explained. Our work provides the insight into the mechanism of low thermal conductivity in thermoelectric materials.

ACKNOWLEDGMENTS

This work was supported by the National Natural Science Foundation of China (Grants No. U21A2079 and No. 52272254), Zhejiang Provincial Key R&D Program of China (Grant No. 2021C01026), Youth Innovation Promotion Association CAS (Grant No. 2019298), and Zhejiang Provincial High-level Talent Special Support Plan (Grant No. 2020R52032).

- [1] J. He and T. M. Tritt, *Science* **357**, eaak9997 (2017).
- [2] G. D. Mahan and J. O. Sofo, *Proc. Natl. Acad. Sci. USA* **93**, 7436 (1996).
- [3] I. T. Witting, T. C. Chasapis, F. Ricci, M. Peters, N. A. Heinz, G. Hautier, and G. J. Snyder, *Adv. Electron. Mater.* **5**, 1800904 (2019).
- [4] H. Tamaki, H. K. Sato, and T. Kanno, *Adv. Mater.* **28**, 10182 (2016).
- [5] J. P. Heremans, V. Jovovic, E. S. Toberer, A. Saramat, K. Kurosaki, A. Charoenphakdee, S. Yamanaka, and G. J. Snyder, *Science* **321**, 554 (2008).
- [6] L.-D. Zhao, C. Chang, G. Tan, and M. G. Kanatzidis, *Energy Environ. Sci.* **9**, 3044 (2016).
- [7] J. Li, X. Zhang, Z. Chen, S. Lin, W. Li, J. Shen, I. T. Witting, A. Faghaninia, Y. Chen, A. Jain, L. Chen, G. J. Snyder, and Y. Pei, *Joule* **2**, 976 (2018).
- [8] H. Xie, Y. Liu, Y. Zhang, S. Hao, Z. Li, M. Cheng, S. Cai, G. J. Snyder, C. Wolverton, C. Uher, V. P. Dravid, and M. G. Kanatzidis, *J. Am. Chem. Soc.* **144**, 9113 (2022).
- [9] X. Su, N. Zhao, S. Hao, C. C. Stoumpos, M. Liu, H. Chen, H. Xie, Q. Zhang, C. Wolverton, X. Tang, and M. G. Kanatzidis, *Adv. Funct. Mater.* **29**, 1806534 (2019).
- [10] J. Zhang, R. Liu, N. Cheng, Y. Zhang, J. Yang, C. Uher, X. Shi, L. Chen, and W. Zhang, *Adv. Mater.* **26**, 3848 (2014).
- [11] H. Xie, S. Hao, S. Cai, T. P. Bailey, C. Uher, C. Wolverton, V. P. Dravid, and M. G. Kanatzidis, *Energy Environ. Sci.* **13**, 3693 (2020).
- [12] Y. Qin, P. Qiu, R. Liu, Y. Li, F. Hao, T. Zhang, D. Ren, X. Shi, and L. Chen, *J. Mater. Chem. A* **4**, 1277 (2016).
- [13] J. Zhang, L. Huang, C. Zhu, C. Zhou, B. Jabar, J. Li, X. Zhu, L. Wang, C. Song, H. Xin, D. Li, and X. Qin, *Adv. Mater.* **31**, 1905210 (2019).
- [14] Y. Zhu, Y. Liu, M. Wood, N. Z. Koocher, Y. Liu, L. Liu, T. Hu, J. M. Rondinelli, J. Hong, G. J. Snyder, and W. Xu, *Chem. Mater.* **31**, 8182 (2019).
- [15] Y. Cao, X. Su, F. Meng, T. P. Bailey, J. Zhao, H. Xie, J. He, C. Uher, and X. Tang, *Adv. Funct. Mater.* **30**, 2005861 (2020).
- [16] Y. Zhu, B. Wei, J. Liu, N. Z. Koocher, Y. Li, L. Hu, W. He, G. Deng, W. Xu, X. Wang, J. M. Rondinelli, L.-D. Zhao, G. J. Snyder, and J. Hong, *Mater. Today Phys.* **19**, 100428 (2021).
- [17] H. Xie, E. S. Bozin, Z. Li, M. Abeykoon, S. Banerjee, J. P. Male, G. J. Snyder, C. Wolverton, S. J. L. Billinge, and M. G. Kanatzidis, *Adv. Mater.* **34**, 2202255 (2022).
- [18] J. E. Jaffe and A. Zunger, *Phys. Rev. B* **29**, 1882 (1984).
- [19] J. P. Perdew, K. Burke, and M. Ernzerhof, *Phys. Rev. Lett.* **77**, 3865 (1996).
- [20] F. Tran and P. Blaha, *Phys. Rev. Lett.* **102**, 226401 (2009).
- [21] A. Togo and I. Tanaka, *Scr. Mater.* **108**, 1 (2015).
- [22] K. Parlinski, Z. Q. Li, and Y. Kawazoe, *Phys. Rev. Lett.* **78**, 4063 (1997).
- [23] W. Li, J. Carrete, N. A. Katcho, and N. Mingo, *Comput. Phys. Commun.* **185**, 1747 (2014).
- [24] A. Ward and D. A. Broido, *Phys. Rev. B* **81**, 085205 (2010).
- [25] P. Carruthers, *Rev. Mod. Phys.* **33**, 92 (1961).
- [26] See Supplemental Material at <http://link.aps.org/supplemental/10.1103/PhysRevB.107.115202> for additional crystallographic information and calculation results.
- [27] J. D. Beasley, *Appl. Opt.* **33**, 1000 (1994).
- [28] J. Yao, N. J. Takas, M. L. Schliefer, D. S. Paprocki, P. E. R. Blanchard, H. Gou, A. Mar, C. L. Exstrom, S. A. Darveau, P. F. P. Poudeu, and J. A. Aitken, *Phys. Rev. B* **84**, 075203 (2011).
- [29] I. V. Bodnar, *Semiconductors* **37**, 1247 (2003).
- [30] J. D. Burnett, O. Gourdon, K. G. Ranmohotti, N. J. Takas, H. Djieutedjeu, P. F. Poudeu, and J. A. Aitken, *Mater. Chem. Phys.* **147**, 17 (2014).
- [31] G. A. Slack, *Solid State Physics* (Elsevier, New York, 1979), Vol. 34, pp. 1–71.
- [32] P. Villars and K. Cenzual, *Springer-Verlag Berlin Heidelberg & Material Phases Data System (MPDS)*, Switzerland & National Institute for Materials Science (NIMS), Japan, <https://materials.springer.com>.
- [33] S. C. Abrahams and J. L. Bernstein, *J. Chem. Phys.* **59**, 5415 (1973).
- [34] K. Yoshino, H. Komaki, T. Kakeno, Y. Akaki, and T. Ikari, *J. Phys. Chem. Solids* **64**, 1839 (2003).
- [35] B. V. Korzun, A. A. Fadzeyeva, K. Bente, W. Schmitz, and S. Schorr, *Cryst. Res. Technol.* **41**, 168 (2006).
- [36] S.-H. Wei and A. Zunger, *Phys. Rev. B* **55**, 13605 (1997).
- [37] Y. Zhang, X. Yuan, X. Sun, B.-C. Shih, P. Zhang, and W. Zhang, *Phys. Rev. B* **84**, 075127 (2011).
- [38] W. Harrison, *Elementary Electronic Structure* (World Scientific, Singapore, 1999).
- [39] G. Zhou and D. Wang, *Phys. Chem. Chem. Phys.* **18**, 5925 (2016).
- [40] L. Xi, Y. B. Zhang, X. Y. Shi, J. Yang, X. Shi, L. D. Chen, W. Zhang, J. Yang, and D. J. Singh, *Phys. Rev. B* **86**, 155201 (2012).
- [41] J. Cai, J. Yang, G. Liu, H. Wang, F. Shi, X. Tan, Z. Ge, and J. Jiang, *Mater. Today Phys.* **18**, 100394 (2021).
- [42] L. Lindsay and D. A. Broido, *J. Phys.: Condens. Matter* **20**, 165209 (2008).
- [43] H. Xie, S. Hao, T. P. Bailey, S. Cai, Y. Zhang, T. J. Slade, G. J. Snyder, V. P. Dravid, C. Uher, C. Wolverton, and M. G. Kanatzidis, *J. Am. Chem. Soc.* **143**, 5978 (2021).
- [44] J. Yang, Y. Wang, H. Yang, W. Tang, J. Yang, L. Chen, and W. Zhang, *J. Phys.: Condens. Matter* **31**, 183002 (2019).